Materials Advances

ROYAL SOCIETY OF CHEMISTRY

PAPER

View Article Online
View Journal | View Issue

Cite this: *Mater. Adv.*, 2020, 1, 2357

Mechanism of visible photon absorption: unveiling of the C_3N_4–ZnO photoactive interface by means of EPR spectroscopy

Erik Cerrato * and Maria Cristina Paganini

Received 25th June 2020,
Accepted 23rd July 2020

DOI: 10.1039/d0ma00451k

rsc.li/materials-advances

This study elucidates the working mechanism upon visible light exposure of the mixed C_3N_4–ZnO material. Structural (XRD), morphological (TEM) and optical (UV-vis spectroscopy) measurements have highlighted the intimate contact established at the interface of the biphasic solid and enhanced photoactivity arising under visible irradiation with respect to the pristine compounds. Electron paramagnetic resonance (EPR) spectroscopy analysis coupled with *in situ* irradiation, performed at 77 K, and supported by accurate simulations, demonstrated that the charge carrier dynamics at the C_3N_4–ZnO interface is governed by a direct *Z*-scheme heterojunction mechanism rather than that of a type-II heterojunction system. The experimental results suggest that the photoexcited electrons in the ZnO conduction band annihilate the holes in the C_3N_4 valence band, as in a solid direct *Z*-scheme system, allowing an improved charge carrier separation and stabilizing both electrons and holes at the best reductive and oxidative potentials, respectively.

1. Introduction

Nowadays, the necessity to find and develop even more powerful systems in the area of heterogeneous photocatalysis is one of the most arduous challenges currently being attempted by researchers. A standard photocatalytic process is based on the exploitation of light energy, hopefully coming from the sun, to promote chemical transformations.[1,2] The reactions in the photocatalytic field range from the decontamination of pollutants in wastewater,[3,4] to the generation of H_2 from the water photo-splitting reaction,[5,6] and the photo-reduction of CO_2 to generate useful chemical compounds (*i.e.* methanol overall);[7,8] all the processes aim to reduce the environmental impact caused by humans through the contamination and the consumption of the planet's resources.[9,10] The materials identified to be the most suitable for photocatalytic applications have been transition metal oxide semiconductors since their intrinsic band structure allows them to induce the promotion of electrons into the conduction band – CB, leaving holes in the valence band – VB; this takes place when an appropriate amount of energy, equal to or higher than the band gap width, is applied to the material.[11] Once at the semiconductor surface, the photo-generated charge carriers, electrons and holes, can facilitate reductive (H_2 photo-production and CO_2 photo-reduction) and oxidative (photo-degradation) redox reactions, respectively; however, the fraction of charge carriers really available for a photocatalytic process is very poor, since the most probable process is electron–hole pair recombination, limiting the amount of free electrons and holes for redox reactions.

The first study on photoactive materials dates back to the 1920s, but we had to wait until the 1960s to see a systematic study of photoactivity regarding transition metal oxide-based semiconductors.[12,13] The work at that time focused mainly on the fact that wider band gap semiconductors exhibited higher activities concerning the reductive and oxidative redox reactions carried out by electrons and holes. It emerged that a larger band gap corresponded to a more negative potential of the CB and a more positive potential of the VB, and, definitively, to a greater reductive and oxidative ability of the photo-induced charge carriers. By the way, a wider band bap requires higher energy photons for the photoexcitation, belonging to the UV range, which is just 5% of the total solar spectrum at the surface of the earth.[14] On the other hand, the use of semiconductor materials enables the absorption of photons in the visible range ($\lambda > 400$ nm), which forms a larger amount of solar radiation, displaying minimal loss of redox ability in the oxidation of harmful pollutants and in the reduction of H_2O and CO_2 molecules.[15–17] Two main strategies are followed in order to alter and set the material properties in such a way to ensure the maintenance of a higher absorption quantum efficiency and, at the same time, good band redox potentials and enhanced lifetimes of the photoinduced charge carriers: doping and the formation of heterojunctions. The doping procedure

Dipartimento di Chimica, Università di Torino and NIS Center, Via P. Giuria 7, 10125 Torino, Italy. E-mail: erik.cerrato@unito.it

involves the deliberate insertion of a controlled amount of foreign atoms inside a semiconductor matrix leading to the generation of defective states inside the material band gap, allowing the absorption of a major part of the visible solar spectrum.[18–21] The principle issue of this approach lies in the fact that the defective levels can act as charge carrier traps, preventing the availability of the electrons and holes in the CB and VB.

The formation of heterojunctions at semiconductor interfaces results in band alignment, which can occur in different manners depending on the band potentials. The best performance for this technology has turned out to be for interfaced systems in which the band gaps of the semiconductors are staggered with the subsequent improvement of the charge carrier separation,[22] as depicted in Scheme 1; this development has gone down in history as the type-II heterojunction.

The enhanced photocatalytic achievements reside in the fact that the photo-generated charge carriers are stabilized on two different semiconductors, achieving limited electron–hole pair recombination. An inherent restriction of this model is that the holes and electrons are not stabilized on semiconductors with the best oxidative and reductive potentials, respectively. This problem has recently been overcome by the so called "direct *Z*-scheme" or "*S*-scheme" heterojunction, already conceptually theorized by Bard in 1979:[23] the first direct *Z*-scheme-interfaced systems could only be constructed in the liquid phase, since they needed the presence of an electrolytic mediator.[24] In 2006, Tada *et al.*[25] demonstrated that an all-solid *Z*-scheme was possible, in which the solid electron mediator was represented by gold particles. However, it was just in 2013 that direct *Z*-scheme heterojunction engineering was proposed, flanking two semiconductors without electron mediators,[26] whose charge carrier dynamics is sketched in Scheme 2.

The novel technology is achieved, similarly to a type-II heterojunction, when two semiconductors characterized by staggered band gaps are put in contact; but this time, a suitable work function, an intrinsic feature of the two materials, allows the formation of a peculiar electric field at the interface. Due to the existence of an internal electric field coming from the different work functions of the two semiconductors (b) and (c) in Scheme 2, the selective recombination of photoinduced

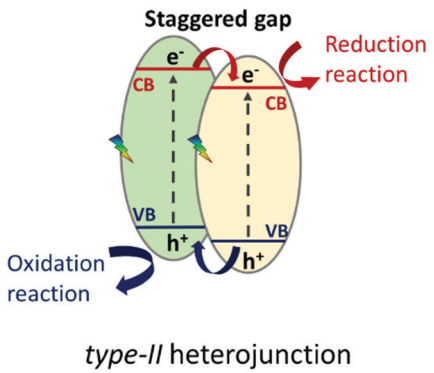

Scheme 1 Type-II heterojunction. Charge carrier separation model at the semiconductor interface characterized by staggered band gaps.

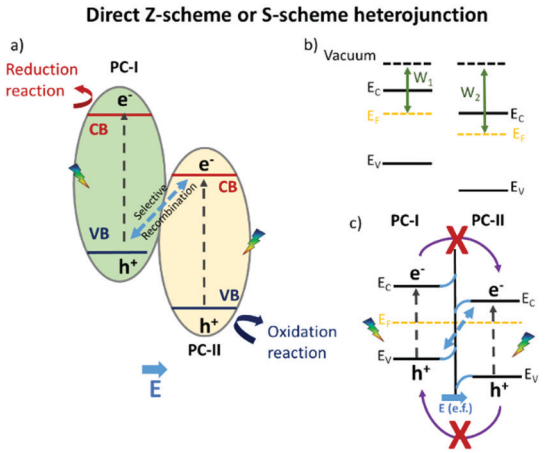

Scheme 2 Interface charge carrier migration in a "direct *Z*-scheme" or "*S*-scheme" heterojunction.

electrons in the semiconductor with the lower CB (PCII) and the holes in the semiconductor with the higher VB (PCI) occurs. This still guarantees the spatial separation of the photoinduced charge carriers that, different from the classical type-II heterojunction, are available at the best redox potentials.[27–29]

In the last decade, the long-time known material g-C_3N_4 has come back into the limelight in the field of heterogeneous photocatalysis. Indeed, although it was first synthetized in 1834 by Berzelius and Liebig,[30] it was only proposed as a suitable polymeric semiconductor for photocatalytic applications, based on earth-abundant elements, in 2009 by Wang *et al.*[31] In their study, the researchers proved the unique photocatalytic ability of g-C_3N_4, derived by the direct heating of a cyanamide precursor in air at different temperatures, in the production of H_2 from the water photo-splitting process upon visible light irradiation. As a matter of fact, the growing interest in the promising photocatalytic performance shown by the metal-free visible active polymeric g-C_3N_4 resulted in almost a quarter of the overall photocatalysis research literature focusing on this subject in 2019. However, despite the undoubted promising properties characterizing a promising photocatalyst exhibited by g-C_3N_4, such as a band gap capable of absorbing visible photons of 2.7 eV,[31,32] modification ability of the band gap through thermal treatments[33–35] and a CB potential able to reduce H_2O and CO_2 molecules, some drawbacks have limited its practical application. Indeed, the high electron–hole recombination rate, the low quantum and separation efficiencies and the small specific surface area resulted in large nanoparticles dramatically affecting the photocatalytic performance. Hence, the need to tune in a proper way the material features by means of doping,[36,37] morphological modifications to increase the surface area, tuning the synthesis parameters and employing soft and hard templates[38–41] for the development of intrinsic defects[42,43] and the formation of heterojunctions with other semiconductors such as TiO_2, ZnO and WO_3 has become paramount.[44–48] This last strategy has produced the best results, delaying electron–hole recombination since the photoinduced charge carriers are stabilized on the two different materials.

By the way, several inferences have corroborated the best performance of the g-C_3N_4-based heterojunction systems, most of the time as result of the enhanced photocatalytic reaction. However, the working mechanism, governing the charge carriers separation enhance, remained often unexplained.

In this work, the C_3N_4–ZnO visible photoactive system, with proven ability in photocatalytic oxidation and reduction,[46,47,49–54] has been synthetized and investigated mainly from the optical and electronic points of view. The most used technique for this purpose is electron paramagnetic resonance (EPR) spectroscopy, able to give a deep view of the electronic states of solids, and used to follow charge carrier separation upon *in situ* irradiation and to depict a direct and clear overview of the electron and hole dynamics at the semiconductor interfaces. To the best of our knowledge, this study provides straightforward and unambiguous proof of the direct *Z*-scheme or *S* scheme heterojunction mechanism of the visible photon absorption characterizing the C_3N_4–ZnO mixed system.

2. Materials and methods

2.1 Sample preparation

Melamine ($C_3H_6N_6$) and zinc nitrate hexahydrate ($Zn(NO_3)_2{\cdot}6H_2O$) employed in the preparation of the samples were purchased from Sigma-Aldrich and used without any further purification treatment.

The 50 : 50 C_3N_4–ZnO mixture was synthetized from an aqueous 1 M (V = 20 ml) solution of the respective precursors ($C_3H_6N_6$ and $Zn(NO_3)_2{\cdot}6H_2O$) kept under constant stirring for one hour at room temperature. The sample was further collected and dried at 353 K. The final material was obtained by thermal annealing in air at 823 K for 4 h with a temperature ramp of 5 °C min^{-1}.

The pristine samples of g-C_3N_4 and ZnO were produced following the same procedure adopted for the mixed system.

2.2 Characterization methods

X-ray powder diffraction (XRPD) patterns, acquired to define the structural phases and the crystallinity of the samples, were recorded using a PANalytical PW3040/60 X'Pert PRO MPD diffractometer using a copper Kα radiation source (0.154056 nm). The intensities were obtained in the 2θ range between 10° and 80°. X'Pert High-Source software was used for data handling.

UV-Visible absorption spectra were recorded using a Varian Cary 5 spectrometer, coupled with an integration sphere for diffuse reflectance (DR) acquisition, using Carywin UV/scan software. A sample of PTFE with 100% reflectance was employed as reference. Spectra were recorded in the 200–800 nm range at a scan rate of 240 nm min^{-1} with a step size of 1 nm. The measured intensities were converted using the Kubelka–Munk function. The energy gap has been evaluated using the Tauc plot method.[55]

Transmission electron microscopy analysis was performed at our institute, using a high resolution transmission microscope, TEM JEOL JEM-3010, operated at 300 keV. The microscope was equipped with a Gatan US1000 CCD camera and Energy Dispersive Detector OXFORD Software INCA.

The electronic paramagnetic resonance measurements were conducted using a CW-EPR EMX-Bruker spectrometer operating at the X-band (9.5 GHz), equipped with a cylindrical cavity operating at 100 kHz field modulation and interfaced with a computer with the WINEPR Acquisition program. The spectra were recorded in a bath of liquid nitrogen (77 K). Prior to the measurements, the samples underwent an activation treatment, aimed at cleaning the surface from absorbed and physisorbed species (hydroxyl and carboxyl groups), obtaining a more stoichiometric compound at the surface, and allowing a more efficient study of the charge carrier separation. The treatment provides a first annealing step in which the materials were heated in a dynamic vacuum at 573 K for 30 minutes; following this, 50 mbar of molecular oxygen was added and the temperature was raised up to 673 K. At the end of the treatment, the excess molecular oxygen was removed and the measurements were performed under a vacuum condition. The photoactivity of the synthetized material was investigated by using coupled EPR spectroscopy with *in situ* irradiation, using a 1000 W xenon lamp (Oriel Instruments) equipped with an IR water filter, to which different band pass filters (Newport-20CGA, UV filter cutting visible light components, $\lambda \geq 400$ nm, $\lambda \geq 420$ nm and $\lambda \geq 455$ nm) were applied. Computer simulation of the EPR spectra was performed using the SIM32 software developed by Prof. Sojka (Jagellonian University, Cracow, Poland).[56]

3. Results

3.1 Structural and morphological analysis

XRPD analysis was executed on the synthetized samples and is reported in Fig. 1, which displays the bare ZnO reflections corresponding to the (100), (002), (101), (102), (110), (103), (200), (112), (201), (004) and (104) planes, typical of the wurtzitic hexagonal crystal phase (JCPDS 36-1451);[57] the reflection sharpness and the absence of further signals confirm the highly pure and crystalline nature of the sample. The diffractogram related to the pure g-C_3N_4 material is characterized by two reflections at 2θ = 27.3° and 2θ = 13.2°, respectively (JCPDS 87-1526): the first one, with the strongest intensity, is associated with the (002) crystal planes of the conjugated stacking aromatic system typical of graphitic materials[38,58] with a distance of 0.326 nm, while the second reflection, weaker and broader, is attributed to the (100) crystal planes of the in-plane structural packing motif of the tri-*s*-triazine (melem) units.[59]

The diffractogram of the 50 : 50 C_3N_4–ZnO mixture reveals a significant change considering the XRPD patterns of both pristine samples, where the g-C_3N_4 structural fingerprints are not present and the reflections of the ZnO phase are considerably reduced, forming a broader profile; however, a 2θ shift was recorded, indicating the existence of unmodified wurtzitic ZnO phase in the mixed sample without the incorporation of external species. Accordingly, the lower intensity and the larger width of the reflections represent a smaller crystal size and a

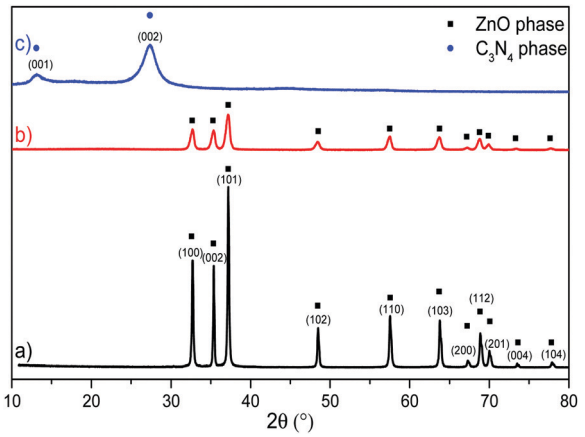

Fig. 1 XRPD analysis of: (a) bare ZnO (black line), (b) g-C_3N_4–ZnO (50 : 50 mixture) (red line) and (c) bare g-C_3N_4 (blue line).

loss in crystallinity in the case of the two-phase systems compared to those of the bare ones. The reduced crystallinity of the mixed material is ascribable to the concurrent crystallization of ZnO that hinders the condensation process and the interlayer stacking of the g-C_3N_4 phase; in contrast, the growth of the ZnO nanocrystals is also delayed by the presence of g-C_3N_4.[50,53]

The TEM pictures acquired for the mixed material, shown in Fig. 2, allow the verification of the existence of the C_3N_4 phase, undetectable by XRPD, and its intimate contact with the ZnO phase.

As shown in Fig. 2(a), the C_3N_4 phase in the mixed system appears as petal brushstrokes painted on the surface of ZnO nanoparticle structures. At higher magnitudes (Fig. 2(b)), ZnO nanocrystals surrounded by the typical multilayer staking structure of the graphitic carbon nitride can be recognised, confirming that the synthetic procedure has enabled the formation of an interfaced system: as will be presented in the following sections, the occurrence of such a connection between the two semiconductors leads to a unique form of charge carrier transport.

3.2 Optical characterization

UV-vis DR spectroscopy has been employed to evaluate the optical behaviour and the electronic structure of the synthetized materials. The semiconducting nature of ZnO, characterized by a direct band gap, appears in spectrum (a) of Fig. 3 with the typical absorption in the UV range up to 375 nm. As widely reported in previous works, it is caused by the electron transition from the valence band, mainly formed by 2p orbitals of O_2^-, to the conduction band, made up by the 4s states of Zn^{2+}. The band gap value, calculated with the Tauc plot method,[55] is in line with those found in the literature and evaluated to be 3.3 eV.[60–65] As reported in previous studies, the direct poly-condensation of the melamine precursor performed at 823 K in air produces C_3N_4 in the graphitic phase, with a band gap of 2.7 eV, making it a material able to absorb photons in the visible range, up to almost 460 nm.[31,32,34,66–68] The UV-vis spectrum (c) in Fig. 3 shows this feature, in which the electrons in the VB, predominantly constituted by the p_z orbitals of nitrogen, are photoexcited by visible photons, up to energies corresponding to wavelengths around 460 nm, into the conduction band, composed of the p_z orbitals of carbon atoms.

Concerning the optical analysis of the 50 : 50 mixed system (spectrum b), (Fig. 3), it exhibits a red-shift of the absorption edge with a band gap value of 3.1 eV with respect to that of pristine ZnO, where the visible photon absorption improvement is attributed to the presence of the C_3N_4 phase, suggesting a close cooperation of the two phases at the interface. The zoomed-in view shown in Fig. 3 ascertains that the mixed material shows a slightly higher absorption of photons at longer wavelengths compared with bare g-C_3N_4, probably due to the higher defectiveness of this phase in the mixed system as a result of the simultaneous crystallization with the ZnO phase during C_3N_4 condensation, as already discussed in previous works.[37,49,50,52] It should be noted that the absorption of the C_3N_4–ZnO interface is higher also in the UV range with respect to g-C_3N_4, thanks to the presence of ZnO. Then, it can be attested that the contemporary presence of the two phases is beneficial in terms of there being a wider range of photons absorbed with respect to the bare materials, both in the UV and visible ranges, revealing an intimate cooperation of the two phases during the light absorption determined by a successful charge carrier transfer at the interfaces.

3.3 EPR spectroscopic study upon exposure to irradiation

In general, electron paramagnetic resonance (EPR) spectroscopy is a highly sensitive magnetic resonance technique based

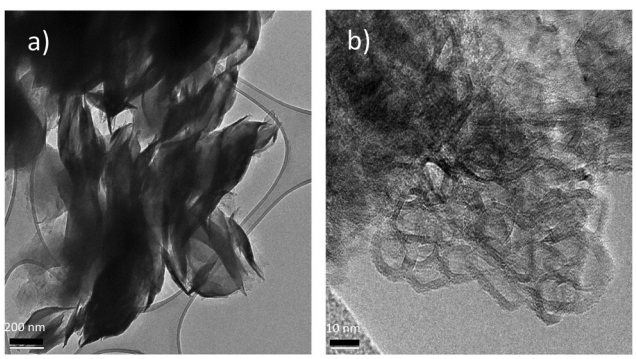

Fig. 2 TEM images of C_3N_4–ZnO (50 : 50).

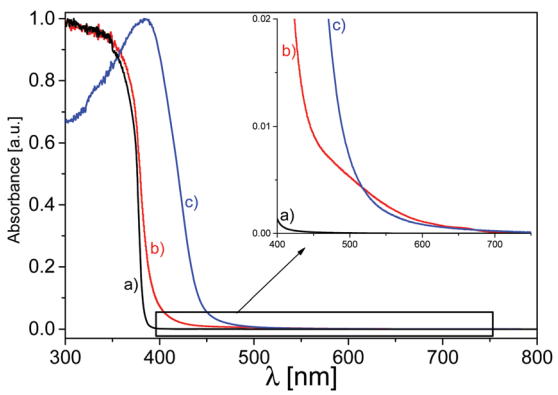

Fig. 3 Normalized UV-vis DR spectroscopy measurements of: (a) pristine ZnO (black line), (b) C_3N_4–ZnO (50 : 50) (red line) and (c) g-C_3N_4 (blue line).

on the energy separation of the spin states of an unpaired electron by the action of an external magnetic field, exploiting the electronic Zeeman effect, in which the magnetic transitions are induced by microwave photons (in the range of GHz). In the last decades, its potentiality in the huge panorama of heterogeneous catalysis has increased, with particular emphasis in the field of photocatalysis.[69,70] This has been possible since EPR has proven to be a sensitive tool for the monitoring of charge carrier separation, with the carriers very often trapped in intrinsic or extrinsic defect sites during light absorption, generating paramagnetic species. In this sense, EPR can be considered as an analytical technique that can be used to perform a pre-screening of material photoactivity.[71,72] In addition, it is increasingly used to obtain supporting analysis to determine the working mechanism upon light absorption of complex materials or heterojunctions,[73–75] in such a way as to achieve the correct electronic transfer at the interface, as will be presented in the following.

Connecting the discussion to transition metal oxide semiconductors, it is well known that, considering the band structure whereby they are modelled, when a semiconducting material is irradiated by a suitable light energy, the excitation of electrons (negatively charged) from the valence band to the conduction band occurs, leaving the holes (positively charged) in the valence band and generating charge carrier separation; this phenomenological occurrence is reported in eqn (1):

$$MeO_X + h\nu \rightarrow e_{(CB)}^- + h_{(VB)}^+ \quad (1)$$

In this regard, when the irradiation is conducted under vacuum conditions (where no surface molecules can interact with the excited charge carriers) and at a low enough temperature, such as that of liquid nitrogen (77 K, to prevent electron–hole pair recombination), it is possible to follow the photo-generation of electrons and holes that, stabilized in the solid, induce paramagnetic species peculiar to each solid.

As is obvious, the stabilization of photo-generated charge carriers depends on the nature of the oxide matrix, but some guidelines can be summarized. The photoexcited electrons are generally stabilized on metal cations, as described by eqn (2), forming shallow donor energetic levels just below the conduction band edge.

$$Me^{n+} + e^- \rightarrow Me^{n-1} \quad (2)$$

In this way, the ionized metal cation becomes a paramagnetic centre, easily recognizable *via* EPR.

On the other hand, the photoinduced holes are stabilized at the oxygen ions of the lattice (O^{2-}), ionizing them to the paramagnetic species O^-, as outlined hereafter in eqn (3):

$$O^{2-} + h_{(VB)}^+ \rightarrow O^- \quad (3)$$

Transferring the acquired knowledge to the materials of this study, in Fig. 4, the EPR spectrum of pristine ZnO after the activation process (see Materials and methods section) is shown before and during the exposure to UV light irradiation. As confirmed by the UV-vis spectra(Fig. 3), the synthetized ZnO

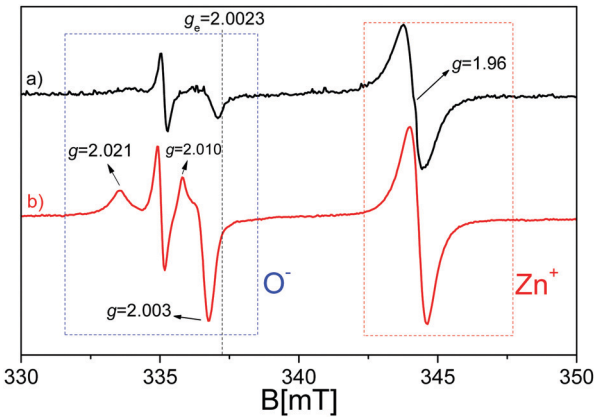

Fig. 4 EPR spectra of pristine ZnO recorded at 77K and in a vacuum after the activation treatment: (a) in the dark (black line) and (b) upon UV irradiation (red line).

is photoactive just in the UV range of the electromagnetic spectrum, with no activity under visible light. The spectrum (a) of Fig. 4 shows that ZnO displays some EPR signals before the illumination procedure, due to the lack of a perfect stoichiometry in the sample, where, in order to maintain charge neutrality, several defects are generated, among which some have paramagnetic character. Upon UV exposure, the profile of the spectrum does not change qualitatively, but one witnesses an intensity increase of the EPR signals. In detail, the quasi-isotropic line with $g < g_e$ (right hand side of the spectra, g_e = 2.0023 is the free electron g value) at g = 1.96 is caused by electrons excited in the conduction band and relaxed in shallow donor levels, at around 0.02–0.05 eV below the conduction band edge. The shallow donor nature has been, in the past, the subject of several different attributions among which are oxygen vacancies (or *F*-centres),[76–78] interstitial zinc,[79–84] group-III element impurities[85–87] and interstitial hydrogen.[88–90] Although the assignment to oxygen vacancies is nowadays considered erroneous, since the theoretical calculations confirmed their location in the middle of the ZnO band gap instead of being shallow,[65,91] the signal's origin still lacks a clear and defined explanation. An unambiguous answer is complicated by the fact that the isotopic abundance of ^{67}Zn (I = 5/2, giving a six line multiplicity for the hyperfine interaction) is lower than 5%, preventing the observation of any resolved hyperfine interaction that could provide direct information about the chemical nature of the donors. In addition, an isotropic line has been observed in highly pure ZnO single crystals, making the hypothesis that it could be caused by III-group elements less convincing. However, all researchers agree with the fact that the signal at g = 1.96 is derived from the electrons in the conduction band or trapped in the shallow donor levels; in the latter case, the signal seems to be independent of the shallow donor identity[92,93] and the electrons can be modelled in an effective-mass-hydrogenetic-like state.[94]

In line with the above mentioned debate, the signal enhancement upon UV irradiation is attributed to the photoexcitation of electrons from the valence band to the conduction band or in

shallow donor levels. The mechanism reported in eqn (4) is therefore purely formal but consistent with the EPR study of other transition metal oxide semiconductors, where the photoexcited electrons are stabilized on specific cations (*e.g.* Ti^{3+} in TiO_2 and Zr^{3+} in ZrO_2[69,72]).

$$Zn^{2+} + e^- \rightarrow Zn^+ \quad (4)$$

The growth of a complex signal at $g > g_e$ (left-hand side of the spectra) constituted by two axial signals with $g_{\parallel} = 2.019$ and $g_{\perp} = 2.005$ and $g_{\parallel} = 2.010$ and $g_{\perp} = 2.004$ upon irradiation is caused by the trapping of photo-generated holes, taking place according to eqn (3).[78,81,95–98]

After having ascertained that the stabilization of charge carriers upon UV irradiation can be followed *via* EPR spectroscopy for ZnO, we shift the matter of the discussion to the bare g-C_3N_4 semiconductor. Before analysis of the EPR outcomes for the graphitic polymer, it is worth considering its electronic configurations and their hybridization. Considering the carbon in the N=C–N_2 bond of the tri-*s*-triazine ring in the ground state, the 2s orbital is filled with two electrons with opposite spins, as well as the $2p_x$ and $2p_y$ sublevels of the 2p orbitals, while the $2p_z$ orbital is unoccupied. Passing to the excited state, with each of the $2p_x$, $2p_y$ and $2p_z$ orbitals occupied by an unpaired electron, the 2s orbital can hybridize with $2p_x$ and $2p_y$, giving rise to three sp^2 hybridized orbitals (equivalently hybridized), leaving the unpaired electrons in the $2p_z$ state, at slightly higher energy. The same argument can be applied for the N atom in both the C–N=C and in the N–(C)3 bonds: while in the first case, the excited state is characterized by an sp^2 hybridization, this time non-equivalent (one of the three sp^2 hybridized orbitals is doubly occupied) but again with un unpaired electron in the $2p_z$ orbital, in the second case, an equivalent sp^2 hybridization can be considered anew with the $2p_z$ orbital doubly occupied. Having elucidated the atomic configuration in the tri-*s*-triazine unit constituting the heptazine network of g-C_3N_4, the overlapping of the sp^2 hybridized orbitals of C and N atoms results in the formation of σ-bonds, while the overlapping of the $2p_z$ orbitals generates π-bonds. In the latter case, the electrons, half coming from the carbon atoms and half coming from N atom subunits, cannot be confined but they are free, constituting the π-conjugated structure.[99] It should be noted that the two electrons with different spin orientation in the $2p_z$ orbitals of the N atom in the N–(C)3 bonds do not take part in the delocalized π-conjugated system due to the Coulombian repulsion to which they are subjected; in this case, the electrons in the π-conjugated system cannot move in the 2D plane but they can travel inside the triazine ring, leading to a localized π-conjugated structure, as described by DFT calculations in ref. 32.

In light of the clarified atomic configuration characterizing the atoms of the heptazine network constituting the building blocks of the investigated C_3N_4, its EPR spectrum in Fig. 5 can be readily analysed. As reported in many previous works,[33,34,100,101] the spectrum of thermally activated g-C_3N_4, before light exposure, shows an isotropic line with a mostly

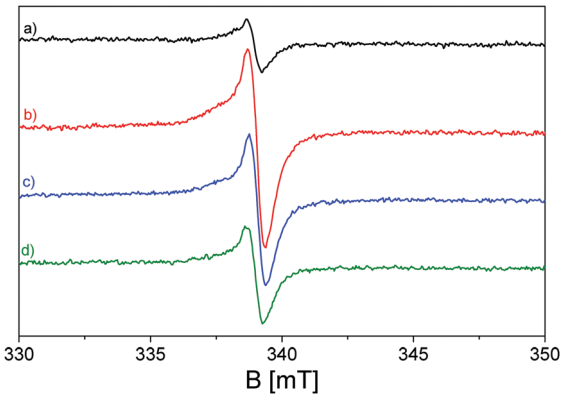

Fig. 5 EPR spectra of pristine g-C_3N_4 recorded at 77 K and in a vacuum after the activation treatment: (a) in the dark (black line), and (b) upon illumination with a band pass filter at $\lambda \geq 400$ nm (red line); (c) at 420 nm (blue line) and (d) at 455 nm (green line).

Lorentzian shape at $g = 2.0042$, caused by unpaired electrons in the localized π-conjugated system, with preferential carbon character; this assignation is supported by the absence of hyperfine splitting typical of unpaired electrons stabilized on N atoms. The presence of unpaired electrons in the localized excited state prior to illumination can be attributed to defects in the nanostructured material caused by melamine polymerization.[99,102,103]

Upon visible light irradiation, performed with several band pass filters at different visible wavelengths of irradiation, the rising up of the Lorentzian line, due to the electron photoexcitation from the valence band (2p nitrogen orbitals) to the conduction band (2p carbon orbitals), dominates the EPR spectra (b–d) of Fig. 5, increasing the number of unpaired electrons in the localized π-conjugated system. It can be observed that the outcomes are in line with the UV-vis spectroscopy measurements (Fig. 3), since the g-C_3N_4 material is still photoactive under irradiation executed with $\lambda \geq 455$ nm, although the intensity of the signal decreases, as can be seen, with increasing irradiation wavelength.

Upon further analysis of the EPR spectra during the irradiation procedure, a further broader shoulder is visible at lower magnetic field values and is attributed to electrons trapped at nitrogen radicals in the polymeric network.[100] In order to evaluate this hypothesis, simulation of the EPR spectra of the g-C_3N_4 sample upon irradiation with $\lambda \geq 400$ nm has been carried out using the SIM32 software:[56] Fig. 6 reports the calculated spectrum in comparison with the experimental one, where the single convolutions are also highlighted.

The simulation confirms the presence of a further species with respect to the most imposing Lorentzian character at $g = 2.0042$ (blue line in Fig. 6), distinguished by a rhombic shaped signal with $g_1 = 2.0150$, $g_2 = 2.0062$ and $g_3 = 2.0012$ (green line in Fig. 6), compatible with the presence of nitroxide species generated during the surface oxidation of the activation treatment.[104–107] The broad profile displayed by the g_1 component of the rhombic signals is imputable to the inhomogeneity

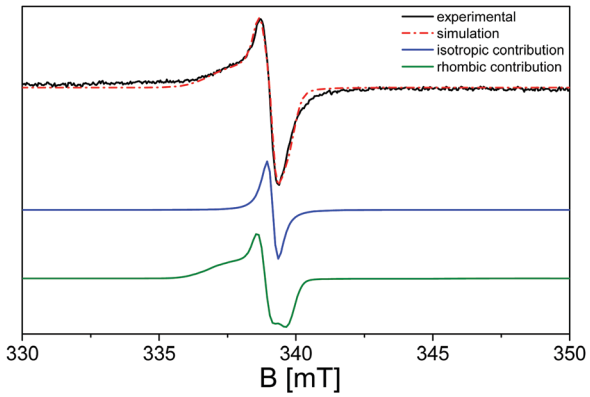

Fig. 6 Simulation of the EPR spectra of pristine g-C_3N_4 recorded at 77 K and in a vacuum after the activation treatment upon illumination at $\lambda \geq 400$ nm: experimental (black line), simulated (red dashed line), Lorentzian convolution (blue line), and rhombic convolution (green line).

of the nanocrystal surface, in which the unpaired electrons can differently interact with the neighbouring species.

Regarding the EPR characterization of the C_3N_4–ZnO mixed system, as shown in Fig. 7, a much more complex profile appears. To the best of our knowledge, this study provides the first investigation of paramagnetic centres regarding the interfaced system C_3N_4–ZnO. In order to streamline the analysis, the first step is to refer back to the EPR features observed for the two bare semiconductors, again by means of a simulation procedure (red line spectrum in Fig. 7).

The various deconvolutions in the calculated spectrum reveal the EPR signals already observed and described for the two separate ZnO and C_3N_4 phases: the spectrum is dominated by the isotropic line at $g = 1.96$ due to electrons trapped in the shallow donor levels of ZnO. The signal at lower magnetic fields appears more complicate with respect to that generated by the trapped holes (O^-) in the pristine ZnO, due to the presence of the Lorentzian signal at $g = 2.0042$ caused by the electrons stabilized at the localized π-bonds, and characterized by the carbon character.

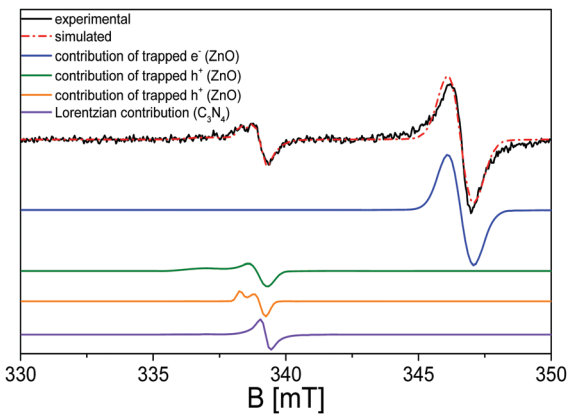

Fig. 7 EPR spectrum of the 50 : 50 C_3N_4–ZnO mixed system and the corresponding simulation: experimental (black line), simulation (red dashed line), contribution from the isotropic line at $g = 1.96$ (trapped electrons) of ZnO (blue line), contribution from the axial line at $g_\parallel = 2.019$ and $g_\perp = 2.005$ (trapped holes) of ZnO (green line), contribution from the axial line at $g_\parallel = 2.010$ and $g_\perp = 2.004$ (trapped holes) of ZnO (orange line), and contribution from the isotropic line at $g = 2.0042$ (trapped electrons) of C_3N_4 (violet line).

The exposure of the mixed material C_3N_4–ZnO to visible irradiation produces a modification of the EPR spectrum in terms of signal intensities completely different with respect to what is observed for the pristine samples. Fig. 8 shows the mixed material upon exposure to light with $\lambda \geq 400$ nm (red line) and $\lambda \geq 455$ nm (blue line).

Opposite to bare ZnO, in which UV irradiation causes a growth of the signal at $g = 1.96$ due to the stabilization of photoexcited electrons in shallow donor levels (Fig. 4), for the mixed sample, the intensity of the signal drops down during the visible light exposure performed with band pass filters at 400 nm and 455 nm. On the other hand, the more complex signals at higher g values, having axial character and attesting to the stabilization of the photoinduced holes stabilized as O^- species in ZnO, grow during irradiation as in the case of the pristine material in the case of UV illumination. Finally, the isotropic Lorentzian line at $g = 2.0042$, caused by the localized electrons in C_3N_4, is embedded in the broader $g_\perp$ component of the O^- centres, as certified by the simulation in Fig. 7 (violet line). This implies that the 50 : 50 C_3N_4–ZnO mixture is photoactive upon visible irradiation, improving the photoactivity feature of the zinc oxide; the observed trend guarantees a beneficial interfacing between the two semiconducting materials in which the charge carrier separation can be analysed and elucidated as discussed in the following section.

3.4 Results and discussion and unveiling of visible photon absorption mechanism

Summarizing the presented results, the synthetized ZnO, characterized by a wurtzitic crystal structure, undergoes charge carrier separation upon UV irradiation that can be followed using EPR spectroscopy by means of well-established strategies, in which the signals of trapped photoinduced charge carriers can be recognized in the spectrum, located in separate spectral regions.[69,70,98] Concerning the pristine g-C_3N_4, obtained by the

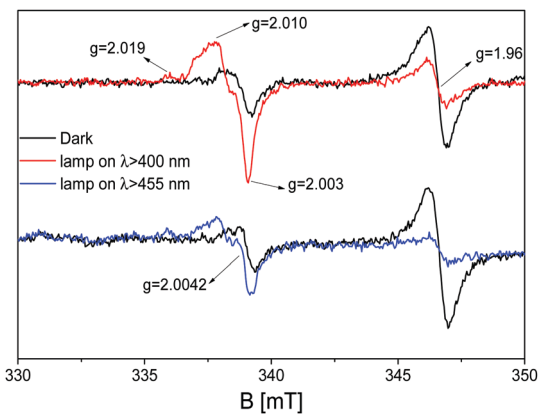

Fig. 8 EPR spectra of pristine g-C_3N_4 recorded at 77 K and in vacuum after the activation treatment: dark (black line), upon illumination with a band pass filter at $\lambda \geq 400$ nm (red line) and at $\lambda \geq 455$ nm (blue line).

poly-condensation of the melamine precursor *via* annealing in air at 823 K, it showed a typical 2D graphitic structure composed of tri-*s*-triazine units dominated by a π-conjugated system. Also, in this case, the excitation of electrons upon visible irradiation has been recognised by means of EPR spectroscopy, with the increase of the Lorentzian line at g = 2.0042 due to the stabilization of excited electrons in the localized π-bonds, having carbon character and forming the material conduction band; moreover, the presence of the surface nitroxide radicals has been verified, having a specific rhombic g-tensor. The activity at different photon frequencies of the two pristine materials was confirmed by means of UV-vis spectroscopy measurements, highlighting the photo absorption of ZnO just in the UV spectral region, while for g-C_3N_4, the absorption edge is around 460 nm. The 50 : 50 mixture has exhibited a red-shift with respect to bare ZnO of the absorption edge and a slightly higher absorption in the visible region compared to that of pure g-C_3N_4, indicating an actual cooperation of the two phases in the interfaced system. TEM imaging confirmed the homogenous distribution of the two phases and their anchoring one around the other, suggesting an active partnership at the interface and constituting a heterojunction system.

In the last years, several authors have reported the prominent photocatalytic ability upon visible light exposure of the mixed C_3N_4–ZnO material,[47,49,54,108,109] where they speculated the working mechanism at the interface of the heterojunction. In most of the cases, the sustained hypothesis of the real process upon visible photonic irradiation foresees an electron transfer from the C_3N_4 conduction band (−1.12 eV *vs.* NHE) to the ZnO conduction band (−0.02 eV *vs.* NHE), typical of a type-II heterojunction or a p–n heterojunction. In contrast, the hole transition would occur from the ZnO valence band (+3.00 eV *vs.* NHE) to the C_3N_4 valence band (+1.57 eV *vs.* NHE) (Scheme 3). In general, in a type-II heterojunction, the spatial charge carrier separation is improved, since the photo-generated charge carriers are localized on the two different semiconductors; however, the stabilized electrons and holes are not at the best potentials for reductive and oxidative redox reactions, respectively. These explanations are not consistent with the extremely high photocatalytic activity exhibited by the C_3N_4–ZnO mixed system in both oxidative and reductive reactions.

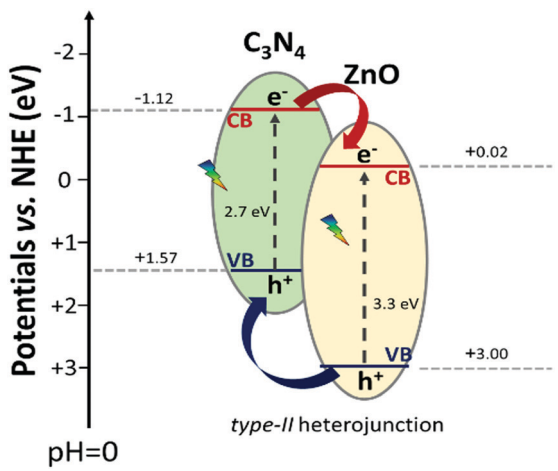

Scheme 3 Schematic representation of the hypothetical C_3N_4–ZnO type-II heterojunction with the standard potential found in the literature.[50]

Accordingly, considering the outcomes of this work obtained by using the EPR technique upon *in situ* visible irradiation of C_3N_4–ZnO and compared with the results of the pure materials, it is clear that a different mechanism of charge carrier migration at the interface should be considered. Indeed, in the case that the working mechanism is the one described above (type-II heterojunction, Scheme 3), the signal at g = 1.96 in the mixed system should grow, in a similar way as in ZnO during UV light exposure, but this is not the case. In contrast, in C_3N_4–ZnO, the signal at g = 1.96 decreases, both with irradiation performed with band pass filters at $\lambda \geq 400$ nm and $\lambda \geq 455$ nm, indicating that an electron transition occurs from ZnO during the illumination; still, the hole signal (O^-), at higher g values, rises in a conspicuous way compared to the holes in bare ZnO, although the irradiation was more energetic (UV) for the pristine material.

This elucidation of the results allows us to sustain the hypothesis proposed by a few researchers, in which they suggested a different electron transition with respect to that of the type-II heterojunction, but without enough convincing mechanistic studies and just derived from photocatalytic reactions.[50] Rather, the charge transfer at the interface of C_3N_4–ZnO during visible light irradiation can be explained with the recently proposed "direct *Z*-scheme or *S*-scheme" heterojunction.[24,29,110,111] In this case, the band alignment configuration at the interface is the same as that of the type-II heterojunction, where the band gaps of the two semiconductors are staggered. The different charge carrier dynamics at the interface is guaranteed by a suitable work function difference at the interface between the two semiconductors, a fundamental prerequisite inducing a specific electric field at the interface. The establishment of the electric field at the interface (derived from the peculiar features of the semiconductors) favours the selective annihilation of the electrons from the semiconductor with the lower conduction band (ZnO in this case) energy and that of the holes from the semiconductor with the higher valence band energy (C_3N_4). The described charge carrier transportation would ensure the strongest redox ability for the photoexcited electrons stabilized in the C_3N_4 conduction band and that of the photo-induced holes in the ZnO valence band, as depicted in Scheme 4.

In conclusion, EPR spectra upon visible irradiation recording both the simultaneous reduction of the electronic signal (g = 1.96) and the improvement of the hole signals of ZnO must be explained by the recombination at the interface of the photo-excited electrons in ZnO with the holes of C_3N_4 (not detected by EPR).

The consistency of these results provides solid proof of the supposed working mechanism occurring during visible irradiation of the C_3N_4–ZnO mixed system, unraveling the predictions of previous studies. Nevertheless, the necessity of a scale-up concerning the production of H_2 from the water photo-splitting

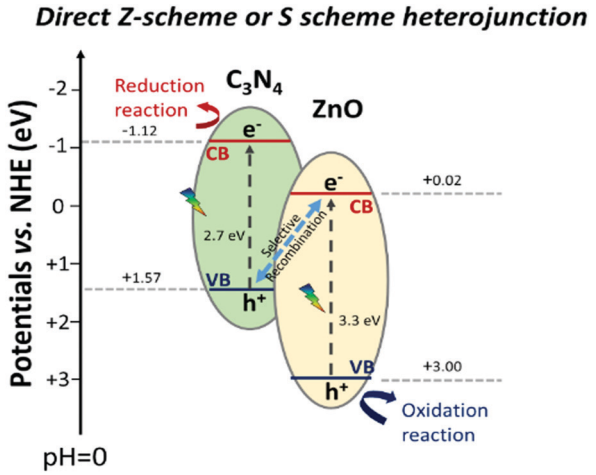

Scheme 4 Schematic representation of the actual C_3N_4–ZnO "direct *Z*-scheme" or "*S* scheme" heterojunction with the standard potential found in the literature.[50]

reaction or CO_2 photo-reduction reaction in chemical products requires further improvements starting from the synthetic routes, aiming obtain more highly porous materials, then with a higher specific surface area available for the reactions at the surface, and to ensure a greater intimate contact at the interface to further enhance the charge carrier annihilation at the semiconductor surfaces.

4. Conclusions

Bare ZnO and C_3N_4 semiconducting materials and the 50 : 50 C_3N_4–ZnO mixture were prepared *via* a fast and facile synthetic route, consisting of a one-step annealing in air of the dissolved precursors at a moderate temperature (823 K) for 5 hours. Structural and morphological analyses have revealed the purity of the obtained phases, expressed in a diffraction pattern of the typical wurtzitic hexagonal phase for ZnO and of the characteristic repetition of the interlayer stacking of the aromatic systems for the C_3N_4 graphitic phase; moreover, the existence of an intimate contact between the two phases for the mixed material emerged, unveiling the formation of an interfaced system. Optical measurements performed with UV-vis DR spectroscopy testified a band gap of 3.3 eV for the bare ZnO and of 2.7 eV for the pristine g-C_3N_4, while the C_3N_4–ZnO sample showed greater light absorption in all the spectral ranges.

The working mechanism upon visible light absorption of the C_3N_4–ZnO heterojunction has been investigated by coupling EPR spectroscopy with *in situ* irradiation performed employing different band pass filters and comparing the outcomes with those of the pristine materials. It was found that bare ZnO displayed an increase of the signals due to the trapping of photoexcited electrons (g = 1.96) and holes ($g_{\parallel}$ = 2.019 and $g_{\perp}$ = 2.005 and $g_{\parallel}$ = 2.010 and $g_{\perp}$ = 2.004), inducing paramagnetic defects; on the other hand, g-C_3N_4 also exhibited an increase of the Lorentzian line at g = 2.0042 upon visible irradiation, caused by the photoexcitation of the electrons from the valence band (with almost nitrogen character) to the conduction band (derived from the p_z carbon orbitals of the π-conjugated system). Concerning the mixed system, opposite behaviour was recorded during visible illumination, where the signal due to the trapped electrons in the ZnO matrices decreased, while the hole signals still increased. The observed phenomenon can only be only explained by assuming a direct *Z*-scheme or *S*-scheme heterojunction at the material interfaces, as previously reported in a few works, and not to a type-II heterojunction as often theorized. To the best of our knowledge, this study provides the first experimental evidence regarding a definitive attribution of the visible light absorption mechanism of the C_3N_4–ZnO heterojunction.

Conflicts of interest

The authors declare no competing financial interest.

Acknowledgements

Financial support from the Italian MIUR through the PRIN Project 20179337R7, MULTI-e "Multielectron transfer for the conversion of small molecules: an enabling technology for the chemical use of renewable energy" is gratefully acknowledged.

Notes and references

1 E. C. C. Baly, I. M. Helilbron and W. F. Barker, *J. Chem. Soc.*, 1921, **119**, 1025–1035.
2 J. M. Coronado, F. Fresno, M. D. Hernández-Alonso and R. Portela, *Design of Advanced Photocatalytic Materials for Energy and Environmental Applications*, London, 2013.
3 D. F. Ollis, E. Pelizzetti and N. Serpone, *Environ. Sci. Technol.*, 1991, **25**, 1522–1529.
4 M. R. Hoffman, S. T. Martin, W. Choi and D. W. Bahnemann, *Chem. Rev.*, 1995, **95**, 69–96.
5 K. Maeda and K. Domen, *J. Phys. Chem. Lett.*, 2010, **1**, 2655–2661.
6 K. Domen, J. N. Kondo, M. Hara and T. Takata, *Bull. Chem. Soc. Jpn.*, 2000, **73**, 1307–1331.
7 T. Inoue, A. Fujishima, S. Konishi and K. Honda, *Nature*, 1979, **277**, 637–638.
8 X. Chang, T. Wang and J. Gong, *Energy Environ. Sci.*, 2016, **9**, 2177–2196.
9 S. Jerez, J. M. Lopez-Romero, M. Turco, P. Jimenez-Guerrero, R. Vautard and J. P. Montavez, *Nat. Commun.*, 2018, **9**, 1304.
10 C. Figures, H. J. Schellnhuber, G. Whiteman, J. Rockström, A. Hobley and S. Rahmstorf, *Nature*, 2017, **546**, 593–595.
11 A. Hernandez-Ramirez and I. Medina-Ramirez, *Photocatalytic Semiconductors*, 2015.
12 L. L. Basov, Y. U. P. Solonitsyn and A. N. Terenin, *Dokl. Akad. Nauk SSSR*, 1965, 122–124.
13 L. L. Basov, G. N. Kuzmin, L. M. Prudnikov and Y. U. P. Solonitsyn, *LGU Leningrad*, 1976, 82–120.

14 K. Ranabhat, L. Patrikeev, A. Antal'evna-Revina, K. Andrianov, V. Lapshinsky and E. Sofronova, *ARPN J. Eng. Appl. Sci.*, 2016, **14**, 481–491.
15 A. V. Emeline, V. N. Kuznetsov, V. K. Ryabchuk and N. Serpone, *Environ. Sci. Pollut. Res.*, 2012, **19**, 3666–3675.
16 N. Serpone and A. V. Emeline, *J. Phys. Chem. Lett.*, 2012, **3**, 673–677.
17 S. Gunti, A. Kumar and M. K. Ram, *Int. Mater. Rev.*, 2018, **63**, 257–282.
18 R. Asahi, T. Morikawa, T. Ohwaki, K. Aoki and Y. Taga, *Science*, 2001, **293**, 269–271.
19 V. C. Anitha, A. N. Banerjee and S. W. Joo, *J. Mater. Sci.*, 2015, **50**, 7495–7536.
20 S. Sato, R. Nakamura and S. Abe, *Appl. Catal., A*, 2005, **284**, 131–137.
21 A. Kudo and Y. Miseki, *Chem. Soc. Rev.*, 2009, **38**, 253–278.
22 H. Wang, L. Zhang, Z. Chen, J. Hu, S. Li, Z. Wang, J. Liu and X. Wang, *Chem. Soc. Rev.*, 2014, **43**, 5234–5244.
23 A. J. Bard, *J. Photochem.*, 1979, **10**, 59–75.
24 J. Low, J. Yu, M. Jaroniec, S. Wageh and A. A. Al-Ghamdi, *Adv. Mater.*, 2017, **29**, 16011694.
25 H. Tada, T. Mitsui, T. Kiyonaga and T. Akita, *Nat. Mater*, 2006, **5**, 782.
26 J. Yu, S. Wang, J. Low and W. Xiao, *Phys. Chem. Chem. Phys.*, 2013, **15**, 16883–16890.
27 J. F. Zhang, Y. F. Hu, X. L. Jiang, S. F. Chen, S. G. Meng and X. L. Fu, *J. Hazard. Mater.*, 2014, **280**, 713.
28 N. Tian, H. Huang, Y. He, Y. Guo, T. Zhang and Y. Zhang, *Dalton Trans.*, 2015, **44**, 4297.
29 Q. Xu, L. Zhang, J. Yu, S. Wageh, A. A. Al-Ghamdi and M. Jaroniec, *Mater. Today*, 2018, **21**, 1042–1063.
30 J. Liebig, *Ann. Pharm.*, 1834, **10**, 172–179.
31 X. Wang, K. Maeda, A. Thomas, K. Takanabe, G. Xin, J. M. Carlsson, K. Domen and M. Antonietti, *Nat. Mater.*, 2009, **8**, 76–80.
32 M. N. Huda and J. A. Turner, *J. Appl. Phys.*, 2010, **107**, 123703.
33 J. Zhang, G. Zhang, X. Chen, S. Lin, L. Mohlmann, G. Dolega, G. Lipner, M. Antonietti, S. Blechert and X. Wang, *Angew. Chem. Int. Ed.*, 2012, **51**, 3183–3187.
34 J. Xiao, Q. Han, H. Cao, J. Rabeah, J. Yang, Z. Guo, L. Zhou, Y. Xie and A. Bruckner, *ACS Catal.*, 2019, **9**, 8852–8861.
35 P. Niu, L. Zhang, G. Liu and H. M. Cheng, *Adv. Funct. Mater.*, 2012, **22**, 4763–4770.
36 M. Bellardita, E. I. Garcia-Lopez, G. Marcì, I. Krivtsov, J. R. Garcia and L. Palmisano, *Appl. Catal., B*, 2018, **220**, 222–233.
37 K. Wang, Q. Li, B. Liu, B. Cheng, W. Ho and J. Yu, *Appl. Catal., B*, 2015, **176**, 44–52.
38 F. Goettmann, A. Fischer, M. Antonietti and A. Thomas, *Angew. Chem., Int. Ed.*, 2006, **45**, 4467–4471.
39 X. Jin, V. V. Balasubramanian, S. T. Selvan, D. P. Sawant, M. A. Chari, G. Q. Lu and A. Vinu, *Angew. Chem., Int. Ed.*, 2009, **48**, 7884–7887.
40 E. Z. Lee, Y. Jun, W. H. Hong, A. Thomas and M. M. Jin, *Angew. Chem., Int. Ed.*, 2010, **49**, 9706–9710.
41 T. Cui, J. Zhang, G. Zhang, J. Huang, P. Liu, M. Antonietti and X. Wang, *J. Mater. Chem.*, 2011, **21**, 13032–13039.
42 D. Zhang, Y. Guo and Z. Zhao, *Appl. Catal., B*, 2018, **226**, 1–9.
43 Y. Li, W. Ho, K. Lv, B. Zhu and S. C. Lee, *Appl. Surf. Sci.*, 2018, **430**, 380–389.
44 X. Liu, N. Chen, Y. Li, D. Deng, X. Xing and Y. Wang, *Sci. Rep.*, 2016, **6**, 6471–6477.
45 L. Kong, X. Zhang, C. Wang, J. Xu, X. Du and L. Li, *Appl. Surf. Sci.*, 2018, **448**, 288–296.
46 J. Zhou, M. Zhang and Y. Zhu, *Phys. Chem. Chem. Phys.*, 2014, **16**, 17627.
47 J. X. Sun, Y. P. Yuan, L. G. Qiu, X. Jiang, A. J. Xie, Y. H. Shen and J. F. Zhu, *Dalton Trans.*, 2012, **41**, 6756–6763.
48 L. Huang, H. Xu, Y. Li, H. Li, X. Cheng, J. Xia, Y. Xu and G. Cai, *Dalton Trans.*, 2013, **42**, 8606–8616.
49 T. Zhai, C. Wang and D. Liu, *Appl. Surf. Sci.*, 2018, **441**, 317–323.
50 W. Yu, D. Xu and T. Peng, *J. Mater. Chem.*, 2015, **3**, 19936.
51 H. Jung, T. T. Pham and E. W. Shin, *Appl. Surf. Sci.*, 2018, **458**, 369–381.
52 S. Le, T. Jiang, Y. Li, Q. Zhao, Y. Li, W. Fang and M. Gong, *Appl. Catal., B*, 2017, **200**, 601–610.
53 Q. Chen, H. Hou, D. Zhang, S. Hu, T. Min, B. Liu, C. Yang, W. Pu, J. Hu and J. Yang, *J. Photochem. Photobiol., A*, 2018, **350**, 1–9.
54 C. Mahala, M. D. Sharma and M. Basu, *ACS Appl. Nano Mater.*, 2020, **3**, 1999–2007.
55 G. Martra, E. Gianotti and S. Coluccia, in *Metal Oxide Catalysis*, ed. S. D. Jackson and J. S. J. Hargreaves, WILEY-VCH Verlag GmbH & Co. KGaA, Weinheim, 2009, pp. 51–94.
56 A. Adamski, T. Spalek and Z. Sojka, *Res. Chem. Intermed.*, 2003, **29**, 793–804.
57 J. Wróbel and J. Piechota, *Solid State Commun.*, 2008, **146**, 324–329.
58 J. Liu, T. Zhang, Z. Wang, G. Dawsona and W. M. Chen, *J. Mater. Chem.*, 2011, **21**, 14398.
59 S. A. Ansari, M. M. Khan, S. Kalathil, A. Nisar, J. Lee and M. H. Cho, *Nanoscale*, 2013, **5**, 9238–9246.
60 A. Ashrafi and C. Jagadish, *J. Appl. Phys.*, 2007, **102**, 071101.
61 V. Srikant and D. R. Clarke, *J. Appl. Phys.*, 1998, **83**, 5447–5451.
62 D. Vogel, P. Krüger and J. Pollmann, *Phys. Rev. B: Condens. Matter Mater. Phys.*, 1995, **52**, R14316–R14319.
63 O. Zakharov, A. Rubio, X. Blase, M. L. Cohen and S. G. Louie, *Phys. Rev. B: Condens. Matter Mater. Phys.*, 1994, **50**, 10780–10787.
64 P. Erhart and K. Albe, *Phys. Rev. B: Condens. Matter Mater. Phys.*, 2006, **73**, 1152071–1152079.
65 A. Janotti and C. G. V. D. Walle, *Phys. Rev. B: Condens. Matter Mater. Phys.*, 2007, **76**, 165202.
66 I. Papailias, T. Giannakopoulou, T. N. D. Demotikali, T. Vaimakis and C. Trapalis, *Appl. Surf. Sci.*, 2015, **358**, 278–286.
67 W. J. Ong, L. L. Tan, Y. Ng, S. T. Yong and S. P. Chai, *Chem. Rev.*, 2016, **116**, 7159–7329.

68 S. Kumar, S. Karthikeyan and A. F. Lee, *Catalysis*, 2018, **8**, 74.
69 V. Polliotto, S. Livraghi and E. Giamello, *Res. Chem. Intermed.*, 2018, **44**, 3905–3921.
70 M. Chiesa, E. Giamello, S. Livraghi, M. C. Paganini, V. Polliotto and E. Salvadori, *J. Phys.: Condens. Matter*, 2019, **31**, 444001.
71 S. Livraghi, M. C. Paganini, E. Giamello, A. Selloni, C. D. Valentin and G. Pacchioni, *J. Am. Chem. Soc.*, 2006, **128**, 15666–15671.
72 V. Polliotto, E. Albanese, S. Livraghi, P. Indyka, Z. Sojka, G. Pacchioni and E. Giamello, *J. Phys. Chem. C*, 2017, **121**, 5487–5497.
73 E. Cerrato, C. Gionco, M. C. Paganini, E. Giamello, E. Albanese and G. Pacchioni, *ACS Appl. Energy Mater.*, 2018, **1**, 4247–4260.
74 E. Cerrato, C. Gionco, M. C. Paganini and E. Giamello, *J. Phys.: Condens. Matter*, 2017, **29**, 1–7.
75 C. Gionco, M. C. Paganini, E. Giamello, R. Burgess, C. Di Valentin and G. Pacchioni, *J. Phys. Chem. Lett.*, 2014, **5**, 447–451.
76 V. Soriano and D. Galland, *Phys. Status Solidi B*, 1976, **77**, 739.
77 R. Laiho, L. S. Vlasenko and M. P. Vlasenko, *J. Appl. Phys.*, 2008, **103**, 123709–12370910.
78 G. Volkel, A. Poppl and B. Voigtsberg, *Phys. Status Solidi A*, 1988, **109**, 295–299.
79 G. Neumann, *Current Topics in Materials Science*, North Holland, Amsterdam, 1981.
80 V. A. Nikitenko, *J. Appl. Spectrosc.*, 1992, **57**, 783–798.
81 P. H. Kasai, *Phys. Rev.*, 1963, **130**, 989–995.
82 L. S. Vlasenko, *Appl. Mag. Res.*, 2010, **39**, 103–111.
83 K. Leutwein and J. Schneider, *Z. Naturforsch.*, 1971, **26a**, 1236–1237.
84 L. E. Halliburton, N. C. Giles, N. Y. Garces, M. Luo, C. Xu and L. B. A. Boatner, *Appl. Phys. Lett.*, 2005, **87**, 1721081–1721083.
85 R. B. Lal and G. M. Arnett, *J. Phys. Soc. Jpn.*, 1966, **21**, 2734–2735.
86 F. A. La Porta, J. Andrés, M. V. G. Vismara, C. F. O. Graeff, J. R. Sambrano, M. S. Li, J. A. Varela and E. Longo, *J. Mater. Chem. C*, 2014, **2**, 10164–10174.
87 M. Setaka, S. Fujieda and T. Kwan, *Bull. Chem. Soc. Jpn.*, 1970, **43**, 2377–2380.
88 C. Gonzalez, D. Block, R. T. Cox and A. Hervè, *J. Cryst. Growth*, 1982, **59**, 357–362.
89 D. M. Hofmann, A. Hofstaetter, F. Leiter, H. Zhou, F. Henecker, B. K. Meyer, S. B. Orlinskii, J. Schmidt and P. G. Baranov, *Phys. Rev. Lett.*, 2002, **88**, 0455041–0455044.
90 A. Janotti and C. G. Van de Walle, *Nat. Mater.*, 2007, **6**, 44–47.
91 F. Oba, M. Choi, A. Togo and I. Tanaka, *Sci. Technol. Adv. Mater.*, 2016, **12**, 034302.
92 K. Senthilkumar, M. Subramanian, H. Ebisu, M. Tanemura and Y. Fujita, *J. Phys. Chem. C*, 2013, **117**, 4299–4303.
93 S. M. Evans, N. C. Giles, L. E. Halliburton and L. A. Kappers, *J. Appl. Phys.*, 2008, **103**, 043710.
94 N. Kondal and S. K. Tiwari, *Mater. Res. Bull.*, 2017, **88**, 156–165.
95 M. Che and A. J. Tench, *Adv. Catal.*, 1982, **31**, 77–133.
96 R. D. Iyengar, *Adv. Colloid Interface Sci.*, 1972, **3**, 365–388.
97 A. M. Volodin and A. E. Cherkashin, *React. Kinet. Catal. Lett.*, 1982, **20**, 335–338.
98 E. Cerrato, M. C. Paganini and E. Giamello, *J. Photochem. Photobiol., A*, 2020, **397**, 112531.
99 P. Xia, B. Cheng, J. Jiang and H. Tang, *Appl. Surf. Sci.*, 2019, **487**, 335–342.
100 D. Dvoranova, Z. Barbierikova, M. Mazur, E. I. Garcia-Lopez, G. Marcì, K. Luspai and V. Brezov, *J. Photochem. Photobiol., A*, 2019, **375**, 100–113.
101 W. Ho, Z. Zhang, M. Xu, X. Zhang, X. Wang and Y. Huang, *Appl. Catal., B*, 2015, **179**, 106–112.
102 D. Hollmann, M. Karnahl, S. Tschierlei, K. Kailasam, M. Schneider, J. Radnik, K. Grabow, U. Bentrup, H. Junge, M. Beller, S. Lochbrunner and A. Thomas, *J. Chem. Mater.*, 2014, **26**, 1727–1733.
103 M. Caux, F. Fina, J. T. S. Irvine, H. Idriss and R. Howe, *Catal. Today*, 2017, **287**, 182–188.
104 G. Dong, Z. Ai and L. Zhang, *RSC Adv.*, 2014, **4**, 5553–5560.
105 J. P. Blinco, B. A. Chalmers, A. Chou, K. E. Fairfull-Smith and S. E. Bottle, *Chem. Sci.*, 2013, **4**, 3411–3415.
106 A. J. Shakir, D. C. Culita, J. Calderon-Moreno, A. Musuc, O. Carp, G. Ionita and P. Ionita, *Carbon*, 2016, **105**, 607–614.
107 C. Yang, M. Guenzi, F. Cicogna, C. Gambarotti, G. Filippone, C. Pinzino, E. Passaglia, N. T. Dintcheva, S. Carroccio and S. Coiai, *Polym. Int.*, 2016, **65**, 48–56.
108 H. Osman, Z. Su and X. Ma, *Environ. Chem. Lett.*, 2017, **15**, 435–441.
109 S. Raha and M. Ahmaruzzaman, *Chem. Eng. J.*, 2019, **387**, 123766.
110 D. Huang, S. Chen, G. Zeng, X. Gong, C. Zhou, M. Cheng, W. Xue, X. Yan and J. Li, *Coord. Chem. Rev.*, 2019, **385**, 44–80.
111 K. Sayama, K. Mukasa, R. Abe, Y. Abe and H. Arakawa, *J. Photochem. Photobiol., A*, 2002, **148**, 71–77.